CHEMISTRY

A nonferrous ferroptosis-like strategy for antioxidant inhibition–synergized nanocatalytic tumor therapeutics

Chenyao Wu[1,2], Zhonglong Liu[3], Zhixin Chen[1], Deliang Xu[1], Lisong Chen[2], Han Lin[1,4]*, Jianlin Shi[1,2,4]*

Ferroptosis, an emerging type of cell death found in the past decades, features specifically lipid peroxidation during the cell death process commonly by iron accumulation. Unfortunately, however, the direct delivery of iron species may trigger undesired detrimental effects such as anaphylactic reactions in normal tissues. Up to date, reports on the cellular ferroptosis by using nonferrous metal elements can be rarely found. In this work, we propose a nonferrous ferroptosis-like strategy based on hybrid $CoMoO_4$-phosphomolybdic acid nanosheet (CPMNS)–enabled lipid peroxide (LOOH) accumulation via accelerated Mo(V)-Mo(VI) transition, elevated GSH depletion for GPX4 enzyme deactivation, and ROS burst, for efficient ferroptosis and chemotherapy. Both in vitro and in vivo outcomes demonstrate the notable anticancer ferroptosis efficacy, suggesting the high feasibility of this CPMNS-enabled ferroptosis-like therapeutic concept. It is highly expected that such ferroptosis-like design in nanocatalytic medicine would be beneficial to future advances in the field of cancer-therapeutic regimens.

INTRODUCTION

Cell death modes have been extensively investigated in the past decades, which can be roughly classified as apoptosis and nonapoptosis routes (*1*). Recently, ferroptosis, which mainly features iron accumulation and lipid peroxidation (LPO), as a nonapoptotic cell death pathway has aroused extensive concerns due to the intrinsic apoptotic resistance of malignant tumors (*2*, *3*). Unfortunately, however, the direct delivery of iron species may trigger undesired detrimental effects such as anaphylactic reactions in normal tissues (*4*–*7*). Alternatively, oncogenic signaling not only can activate oxidation-related enzymes for reactive oxygen species (ROS) generation but also triggers the up-regulation of antioxidant metabolite of glutathione (GSH) for ROS scavenging (*8*, *9*). By using the overexpressed hydrogen peroxide (H_2O_2) in the tumor microenvironment, the Fe(II)-dominated Fenton reaction is able to produce cytotoxic ROS such as hydroxyl radical (·OH) for cancer cell damage, which has been developed as a typical nanocatalytic medicine for tumor-specific therapy (*10*–*12*). In addition, ROS will lead to the peroxidation of polyunsaturated fatty acid into lipid peroxides (LOOH), further facilitating ferroptosis (*13*, *14*). However, owing to the pH limitation, in addition to Fe(II)-mediated Fenton reaction, other metal ion (e.g., Cu and Mn)–catalyzed Fenton-like reactions for nanocatalytic medicine have been rarely reported (*15*–*17*). In addition to directly causing LPO for ferroptosis, ROS has been reported to be able to regulate the genome to promote ferroptosis in high oxidative stress (*13*), indicating that exogenous ROS could promote ferroptosis.

Redox homeostasis in the tumor microenvironment maintains the overexpression of endogenous GSH up to 10 mM (*18*), which is a key responsive event that eliminates possible reactive oxygen burst and subsequently mitigates oxidative stress–related diseases (*19*, *20*). Hence, the presence of massive reductive GSH in tumor regions will largely counteract the efficacy of therapeutic modalities containing chemodynamic, photodynamic, and sonodynamic therapy (*21*, *22*). Hence, it is of great significance to down-regulate intratumoral GSH for facilitating ROS-induced LPO in ferroptosis treatment. In addition, the activation of defensive glutathione peroxidase 4 (GPX4), an enzyme to directly resist LPO in biomembranes for ferroptosis inhibition by overexpressed GSH, will promote the transformation of highly toxic LOOH to hypotoxic hydroxyl fatty acids (LOH) (*23*–*25*). Hence, inhibiting the activity of GPX4 is another representative approach for accelerating LPO. Therefore, GSH depletion will be the most effective approach to inactivate GPX4 and further augment LPO, finally promoting the ferroptosis of cancer cells (*26*). Although nanocatalytic ferroptosis is mainly concentrated on ferrous-based nanomaterials (*27*, *28*), there are few reports focusing on nonferrous-based ferroptosis-inducing agents, which feature enhanced ROS and inactivated GPX4 (*29*, *30*). The development of a nonferrous ferroptosis-like concept may provide an alternative but effective design strategy to achieve the maximized cell death by integrating synergetic ROS burst and GSH depletion into one nanoplatform for precision ferroptosis cancer therapy.

In this work, we propose a nonferrous ferroptosis-like strategy by constructing a hybrid $CoMoO_4$-phosphomolybdic acid nanosheet (CPMNS) nanoplatform for intratumoral lipid peroxide (LOOH) accumulation and subsequent ROS generation for efficient ferroptosis-directed chemotherapy by a Mo(V)-Mo(VI) transition approach (Fig. 1). The unique components of CPMNSs enable the effective Mo^{6+} reduction by GSH, which results in the concurrent GSH depletion and consequent GPX4 enzyme deactivation; meanwhile, the hybrid CPMNS framework is able to degrade and subsequently release Co^{2+} and Mo^{5+} in response to the acidic/reductive intracellular environment of cancer cells, for Co(II)-catalyzed Fenton-like ·OH production and Russell mechanism–enabled $^1O_2$ emergence, respectively. The detailed biochemical mechanism of LPO promotion by suppressing LOOH reduction has been explored in detail as Mo^{6+} reduction–related GSH depletion for deactivating GPX4 enzyme. Such a redox process accelerates CPMNS degradation

[1]State Key Laboratory of High Performance Ceramics and Superfine Microstructures, Shanghai Institute of Ceramics, Chinese Academy of Sciences, Shanghai 200050, China. [2]Shanghai Key Laboratory of Green Chemistry and Chemical Processes, School of Chemistry and Molecular Engineering, East China Normal University, Shanghai 200062, China. [3]Department of Oral Maxillofacial-Head and Neck Oncology, Shanghai Ninth People's Hospital and College of Stomatology, Shanghai Jiao Tong University School of Medicine, Shanghai 200011, China. [4]Shanghai Tenth People's Hospital, Tongji University School of Medicine, Shanghai 200072, China.
*Corresponding author. Email: jlshi@mail.sic.ac.cn (J.S.); linhan@mail.sic.ac.cn (H.L.)

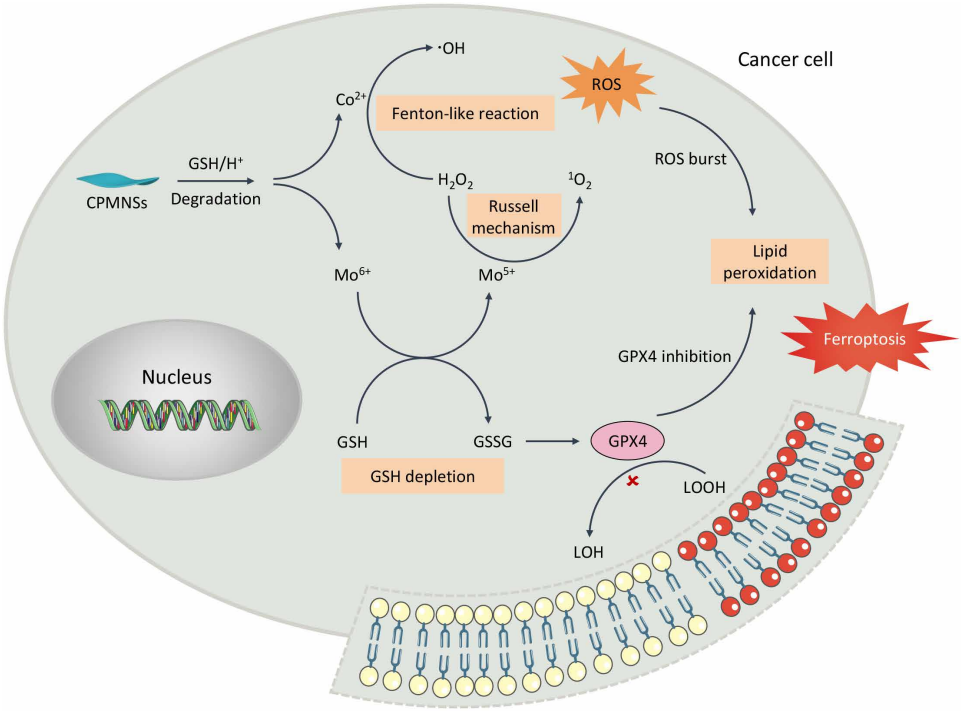

Fig. 1. Nonferrous ferroptosis-like strategy for antioxidant inhibition–synergized nanocatalytic tumor therapeutics. The unique components of CPMNSs enable the effective Mo^{6+} reduction by GSH, which result in the concurrent GSH depletion and consequent GPX4 enzyme deactivation; meanwhile, the hybrid CPMNS framework is able to degrade and subsequently release Co^{2+} and Mo^{5+} in response to the acidic/reductive intracellular environment of cancer cells, for Co(II)-catalyzed Fenton-like ·OH production and Russell mechanism–enabled $^1O_2$ emergence, respectively. Such LPO is promoted by ROS production and GPX4 enzyme deactivation.

for Co ion releasing and further intensifying the ·OH production by Co(II)-involved Fenton-like reaction. The Mo^{6+}-to-Mo^{5+} reduction by GSH renders the $^1O_2$ production by catalyzing H_2O_2 decomposition via a polyoxometalate structure–driven Russell mechanism. Both in vitro and in vivo outcomes demonstrate the markedly enhanced anticancer ferroptosis efficacy, indicating high feasibility of CPMNS-enabled ferroptosis therapeutics for future oncological applications.

RESULTS

Synthesis and characterization of CPMNSs

CPMNSs were prepared by a solvothermal method where the nanosheets exhibit typical sheet-like morphology of ~340 nm in lateral size and ~3.9 nm in thickness (Fig. 2, A and B). The characteristic elemental mapping of CPMNSs shows a well-proportioned distribution of Mo, O, Co, and P (Fig. 2, C and D, and fig. S1). The crystalline structure of CPMNSs was confirmed by x-ray diffraction (XRD) pattern (Fig. 2E), which demonstrates the coexistence of monoclinic $CoMoO_4$ (PDF#21-0868) and cubic polyoxometalate acid ($H_3PMo_{12}O_{40}{\cdot}30H_2O$ of PDF#43-0316 and $H_3PMo_{12}O_{40}{\cdot}xH_2O$ of PDF#43-0314) (*31*). Moreover, x-ray photoelectron spectroscopy (XPS) was adopted to detect the chemical state of CPMNSs. The Co 2p exhibits two main fitting peaks at 796.8 eV (Co $2p_{1/2}$) and 781.1 eV (Co $2p_{3/2}$), which can be assigned to Co^{2+} (Fig. 2F). In addition, the evident peaks at 235.2 eV (Mo $3d_{3/2}$) and 232.1 eV (Mo $3d_{5/2}$) are assigned to the Mo^{6+} (Fig. 2G). The Pluronic F127–modified CPMNSs demonstrate the desired stability in physiological environments, which is confirmed by negligible fluctuation for hydrodynamic size of CPMNSs in both RPMI 1640 medium and fetal bovine serum (FBS) (fig. S2). It can be found that the characteristic peaks of as-modified CPMNSs are compatible with pure Pluronic F127 sample by Fourier transform infrared (FTIR) spectroscopy analysis (fig. S3A). Meanwhile, certain peaks derived from CPMNS skeleton can be assigned to the original phosphomolybdic acid (PMA), demonstrating the independent existence of PMA in CPMNS sample (fig. S3B).

ROS generation and GSH depletion

The Co(II)-mediated Fenton-like reaction was evaluated using a colorimetric method based on the decolorization of methylene blue (MB) after selective ·OH trapping (*32*). Negligible MB absorption change with the CPMNSs + H_2O_2–treated aqueous group could be observed, while an almost complete decay of MB absorption can be found in the group of HCO_3^--assisted CPMNSs + H_2O_2 treatment (Fig. 3A). Therefore, such a physiological HCO_3^-/CO_2 abundance favors the selective ·OH generation by CPMNSs. The electron spin resonance (ESR) spectroscopy experiments further qualitatively confirmed the ·OH production by using 5,5-dimethyl-1-pyrroline *N*-oxide (DMPO) as the spin trap. The distinct ESR signal intensity ratio of 1:2:2:1 of the HCO_3^--assisted CPMNSs + H_2O_2 group suggests the production of ·OH radicals, which is reasoned to be from the Co(II)-enabled Fenton-like reaction in an acidic HCO_3^--support environment (Fig. 3B).

The underlying mechanism of the HCO_3^--facilitated Co(II) Fenton-like reaction illustrates that HCO_3^- species functions as a ligand to chelate metal ions, resulting in redox activity changes marked by different redox potentials (*33*). The electrochemical oxidation of Co^{2+} was depicted in Fig. 3C, where increased HCO_3^- amount

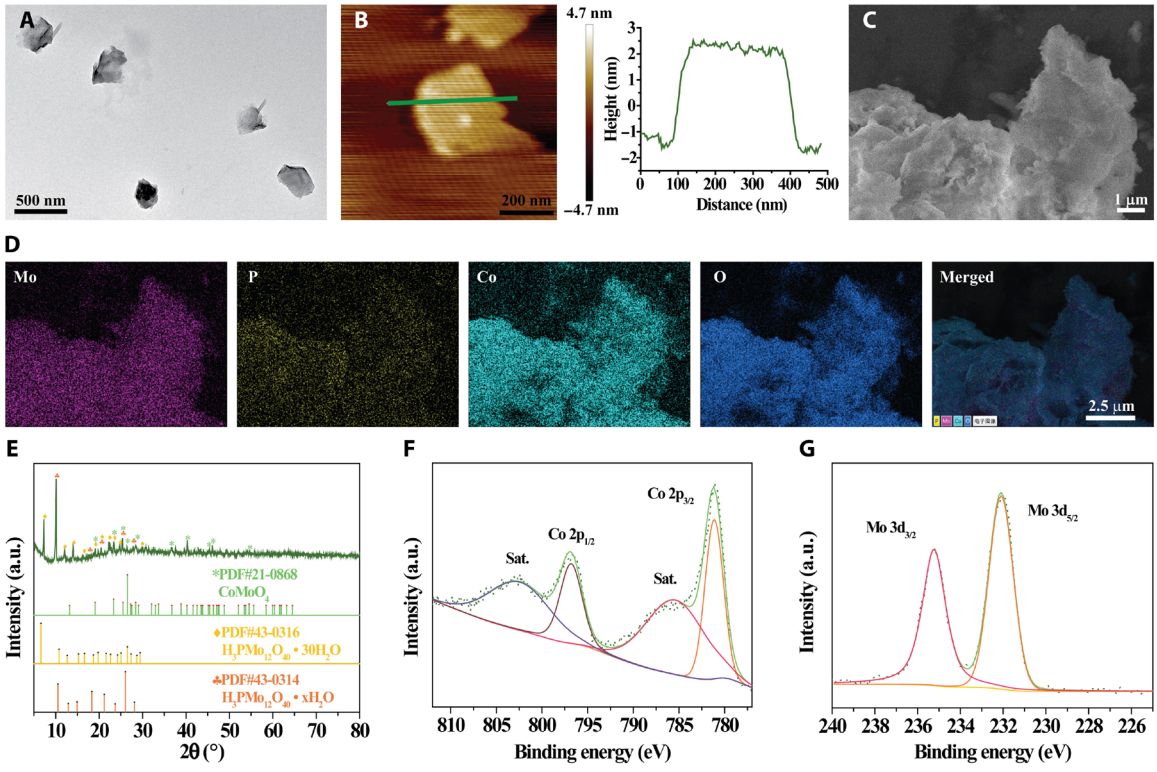

Fig. 2. Characterization of CPMNSs. (**A**) Transmission electron microscopy (TEM) image of CPMNSs. (**B**) Typical atomic force microscopy image and thickness distribution analysis of CPMNSs. (**C**) Scanning electron microscopy (SEM) image and (**D**) the corresponding elemental Mo, P, Co, and O mapping images of CPMNSs. (**E**) XRD pattern of CPMNSs. XPS spectra of (**F**) Co and (**G**) Mo components. a.u., arbitrary units.

results in the gradual decay of the oxidation peak potential, which sensitizes Co^{2+} to catalyze H_2O_2 decomposition for ·OH formation. Such a Co^{2+}-mediated ·OH burst under the assistance of HCO_3^- is expected to trigger in vivo LPO.

The GSH depletion was verified using 5,5′-dithiobis(2-nitrobenzoic acid) (DTNB) based on its specificity to recognize sulfhydryl groups at 412 nm of absorption peak. The 64.2% GSH was consumed by CPMNSs (50 μg ml^{-1}) in 3 hours of reaction, while 96.0% GSH was depleted by H_2O_2 (1 mM) as a positive control group (Fig. 3D and fig. S4A). Besides, more amount of GSH will be depleted by CPMNSs at increased concentration and/or prolonged reaction (fig. S4, B to D). The potential-closed and multiple peak pairs of Mo oxidation/reduction illustrate the rapid and reversible electron transfer performance, i.e., smooth valence state transitions (Fig. 3E) (*34*). The reductant GSH consumption is accompanied by the Mo^{6+} reduction to Mo^{5+}, which has a lower binding energy of 227.3 eV (Mo $3d_{5/2}$) in the XPS spectrum, confirming the existence of Mo^{5+} [Fig. 3E (inset) and fig. S5A]. After subsequent reaction with H_2O_2, the reduction peak of the as-GSH-reduced CPMNSs (noted as ReCPMNSs) of Mo^{5+} disappeared, suggesting Mo^{5+} oxidation into Mo^{6+} (fig. S5B). At last, additional GSH addition effectively reduced Mo^{6+} into Mo^{5+} again, as confirmed by the emerging reduction peak in the lower binding energy of Mo^{5+} (fig. S5C). Such a redox reaction offers two advantages of GSH depletion for LPO promotion and Mo^{5+} formation for $^1O_2$ production.

The ReCPMNS-mediated Fenton-like reaction was further explored. The ROS-induced MB degradation absorption notably declines with the increment of GSH concentrations (0 to 1 mM) compared with that of GSH-free group, implying more ·OH production, which can be attributed to GSH-promoted Co^{2+} release. Unexpectedly, the MB degradation efficiency weakens when GSH is up to 2 mM on account of the ROS scavenging potency of excessive unreacted antioxidant GSH (Fig. 3F). The GSH-stimulated ROS intensification was further investigated. It can be found that the CPMNSs are rapidly degraded with the assistance of GSH in comparison with that of GSH-free group at the same time (fig. S6). After reacting with GSH for 10 min, this GSH-treated CPMNS sample shows evident dissolution and structure collapse, but the GSH-free group presents slight changes. This degradation process also results in the accelerated release of Co^{2+} ions (Fig. 3G). Briefly, in the experimental time interval of 6 hours, the Co^{2+} ion cumulative release amount of ReCPMNSs is 2.3 times higher than that of CPMNSs in phosphate-buffered saline (PBS) (pH 6.5). Thus, this redox reaction destroys the CPMNS microstructure and releases Co^{2+} ions similar to as-reported redox-induced degradation (*16*, *35*). In addition, the Co^{2+} ions release exhibits an evident pH-dependent behavior, which is of high efficiency in the simulated tumor environment of pH 6.5 in comparison to the simulated normal tissues of pH 7.4, suggesting the tumor-specific ferroptosis therapeutics of CPMNSs.

We next examined the $^1O_2$ production from H_2O_2 catalyzed by ReCPMNSs. Singlet oxygen sensor green (SOSG) dye, a specific probe to recognize $^1O_2$, shows elevated fluorescent intensity while the individual ReCPMNSs and H_2O_2 exhibit faint fluorescent signals (Fig. 3H). 1,3-Diphenylisobenzofuran (DPBF) was also used to verify the $^1O_2$ production according to the $^1O_2$-driven DPBF degradation (fig. S7). As depicted in Fig. 3I, ESR spectroscopy confirms

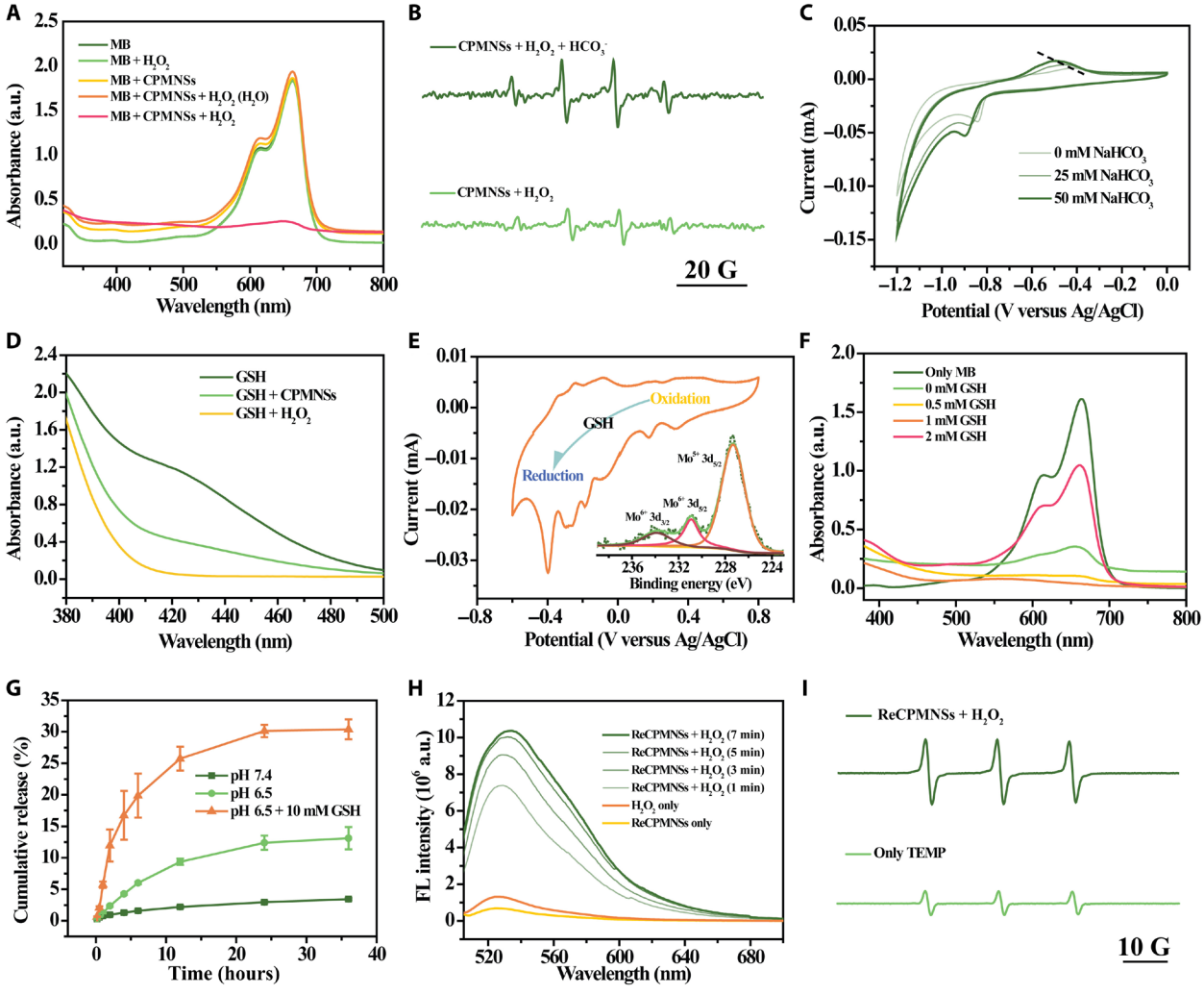

Fig. 3. ROS generation and GSH depletion assay. (**A**) MB degradation by CPMNS-mediated Fenton-like reaction under different conditions in $NaHCO_3/CO_2$ buffer. (**B**) ESR spectra showing the CPMNS-induced ·OH generation with or without HCO_3^-. (**C**) Cyclic voltammetry curves of CPMNSs at varied HCO_3^- electrolyte concentrations. (**D**) GSH depletion by CPMNSs and H_2O_2. (**E**) Cyclic voltammetry curve for molybdenum valence change detection (inset: XPS spectrum of Mo element analysis from ReCPMNSs). (**F**) MB degradation of ReCPMNS-mediated Fenton-like reaction with different GSH concentrations in $NaHCO_3/CO_2$ buffer. (**G**) Cumulative release of Co ion in phosphate-buffered saline (PBS) buffer with or without GSH. (**H**) Singlet oxygen sensor green (SOSG) fluorescent intensity changes with different conditions. (**I**) ESR spectra detection of 2,2,6,6-tetramethylpiperidine (TEMP)–captured $^1O_2$.

the characteristic 1:1:1-signal peak matching $^1O_2$ species by 2,2,6,6-tetramethylpiperidine (TEMP) trapping, implying a marked enhancement of $^1O_2$ in ReCPMNSs and H_2O_2 mixture group in contrast to the blank group. It is depicted that the $^1O_2$ formation can be attributed to the Russell mechanism involving a linear tetraoxide (ROOOOR) (*36*, *37*). Polyoxometalate of ReCPMNSs will react with H_2O_2 to form such a tetraoxide followed by its decomposition to generate $^1O_2$, which alternatively oxidizes Mo^{5+} back to Mo^{6+} (fig. S8). Hence, benefiting from the redox reaction between GSH and CPMNSs and the reversible Mo^{6+}-Mo^{5+} transition, $^1O_2$ can be produced continuously.

In vitro ferroptosis analysis

The cell internalization was evaluated by coincubating 4T1 cells with rhodamine B–labeled CPMNSs. The fluorescence intensities increase with the increasing time duration of coincubation, which demonstrates the effective cell uptake of CPMNSs (fig. S9). To demonstrate ferroptosis-induced cancer cell damage of CPMNSs, typical ferroptosis-related inhibitors were used to validate the ferroptosis-based therapeutic effect at a CPMNS concentration of 150 μg ml^{-1}, which exhibits a relatively low CPMNS concentration for effective cellular ferroptosis (Fig. 4B). Liproxstatin-1 (Lip-1; a typical ferroptosis inhibitor), deferoxamine mesylate (DFOM; a specific iron chelating agent), and EDTA (as a Co ion chelating agent) are able to largely alleviate cellular damage caused by CPMNSs, indicating that the CPMNS-mediated cell death is majorly derived from ferroptosis (Figs. 4C and 5B and fig. S10). Besides, CPMNSs also exhibit the capacity to induce apoptosis because ROS is a key factor to induce apoptosis (fig. S11) (*38*). The inevitable LPO intensification by ferroptosis is mainly achieved through two pathways: the promoted ROS production via Co(II)-mediated Fenton-like reaction and Mo(IV)-driven Russell mechanism and the GPX4

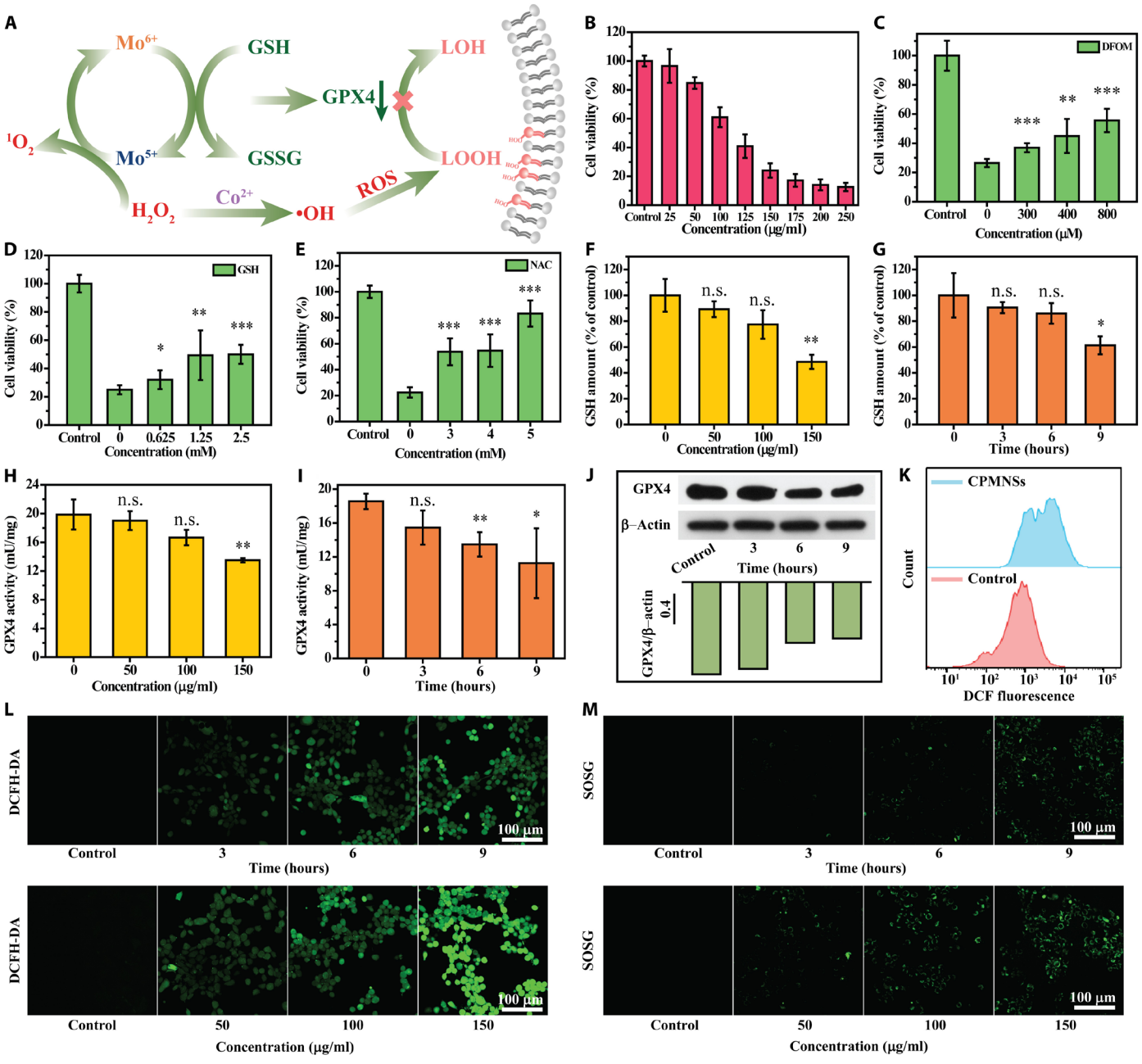

Fig. 4. Intracellular ferroptosis evaluation. (**A**) Schematic illustration of LPO for cellular membrane damage. (**B**) Cell viabilities of 4T1 cells coincubated with different concentrations of CPMNSs. (**C** to **E**) 4T1 cell viabilities by CPMNS treatments in combination with the additions of (C) DFOM, (D) GSH, and (E) NAC. (**F** and **G**) GSH levels of CPMNS-treated cells incubated with CPMNSs of varied (F) concentrations and (G) time intervals. GPX4 activity expression of CPMNS-treated cells incubated with CPMNSs of different (**H**) concentrations and (**I**) time intervals. (**J**) Western blot analysis of GPX4 protein with varied conditions. (**K**) Flow cytometry analysis of DCFH-DA dye-stained 4T1 cells with or without CPMNS treatment. (**L** and **M**) CLSM images of (L) DCFH-DA dye–stained and (M) SOSG dye–stained cells after treatments with CPMNSs of varied concentrations and time intervals. *$P < 0.05$, **$P < 0.01$, and ***$P < 0.001$ of (B) to (E) compared with CPMNS treatment without ferroptosis inhibitors. *$P < 0.05$ and **$P < 0.01$ of (F) to (I) compared with the group without CPMNS incubation. n.s., not significant.

deactivation to prevent the LPO reduction by GSH depletion (Fig. 4A). In general, GSH overexpression in situ tumor tissue meets its growth-required redox homeostasis (*18*), which consumes ROS and activates GPX4 expression, and is therefore regarded as a major obstacle in tumor therapeutics. Hence, GSH marks an important index of cell death. Expectedly, the cell viabilities are enhanced when GSH is supplemented, proving the effect of GSH consumption by CPMNSs on elevating the treatment efficacy (Fig. 4D). Moreover, *N*-acetyl-L-cysteine (NAC), a precursor of GSH biosynthesis (*39*), exhibits the similar protection effect during the CPMNS treatment (Fig. 4E). To quantitatively evidence the GSH consumption, GSH concentration reduction upon CPMNS treatments at varied

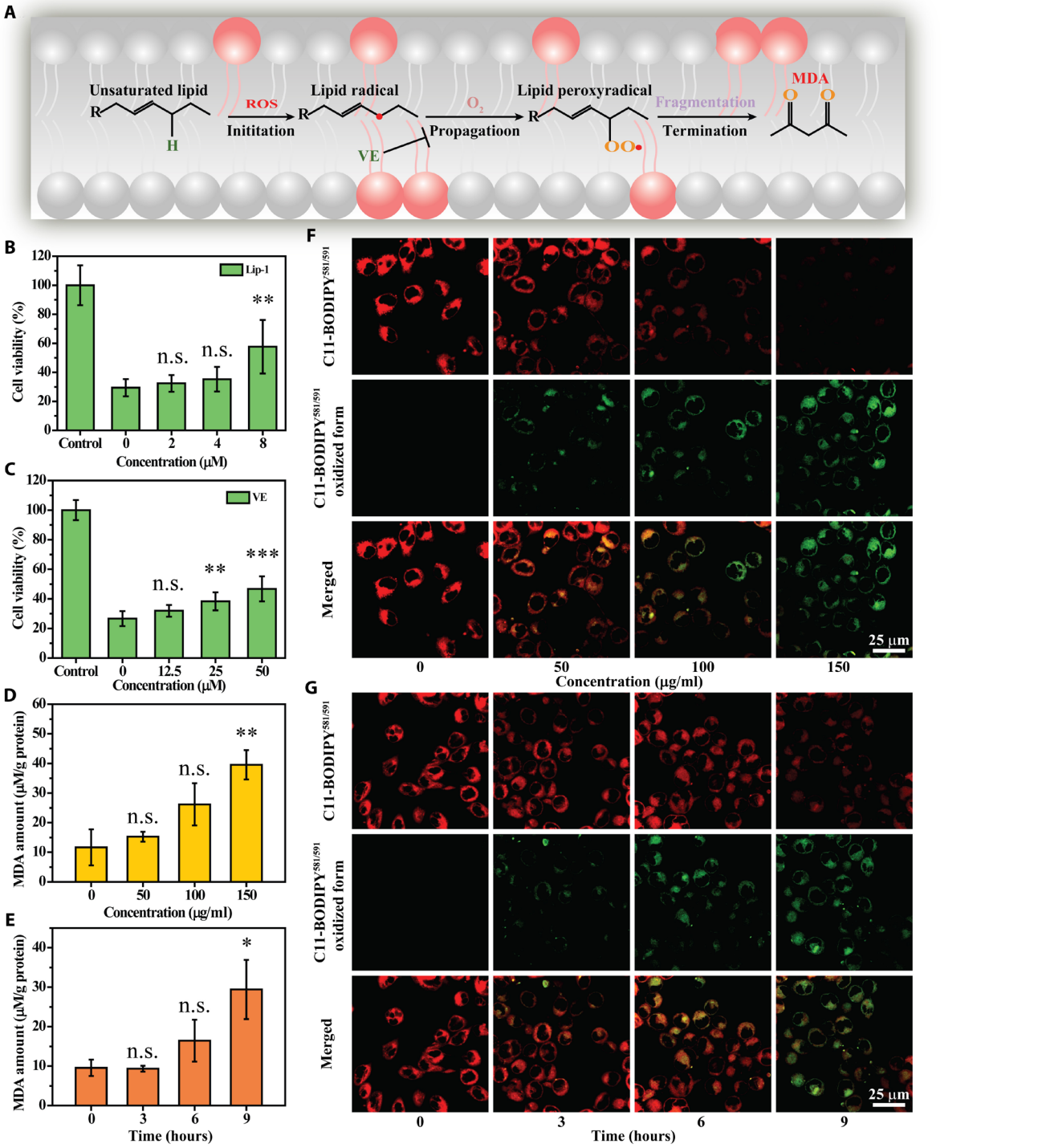

Fig. 5. In vitro LPO of CPMNSs. (**A**) Schematic illustration of LPO process. (**B** and **C**) Cell viabilities of CPMNS-treated 4T1 cells with (B) Lip-1 and (C) VE addition. (**D** and **E**) LPO product MDA detection of 4T1 cells after being incubated with CPMNSs of varied (D) concentrations and (E) time treatments. (**F** and **G**) CLSM images of C11-BODIPY$^{581/591}$ dye–stained 4T1 cells after being incubated with CPMNSs of varied (F) concentrations and (G) time intervals. $^{**}P < 0.01$ and $^{***}P < 0.001$ of (B) and (C) compared with CPMNS treatment without ferroptosis inhibitors. $^{*}P < 0.05$ and $^{**}P < 0.01$ of (D) and (E) compared with the group without CPMNS incubation.

concentrations and durations has been verified, especially compared with the blank group (Fig. 4, F and G). In addition, the presence of intracellular low-valence Mo element implies the GSH depletion, as indicated by the lower binding energy of 227.2 eV (Mo $3d_{5/2}$) of Mo^{5+} (fig. S12). Furthermore, the deactivation of GSH-associated GPX4 was further investigated, which shows much decreased activities upon CPMNS treatments at varied concentrations and durations (Fig. 4, H and I). Such a GPX4 deactivation is highly favorable for blocking the LPO elimination, which suggests largely suppressed defense and repair function of lipid antioxidant and the resultantly

promoted ferroptosis of tumor cells by CPMNSs. In addition, Western blot results also demonstrate a down-regulated expression of GPX4 protein in the time course (Fig. 4J).

Subsequently, oxidative stress triggered by CPMNSs to cellular phospholipid was further assessed. A 2,7-dichlorofluorescein diacetate (DCFH-DA) probe was used to detect the intracellular ROS generation. Flow cytometry analysis presents the enhanced cellular DCF fluorescent signals by CPMNS treatment in 3 hours (Fig. 4K), illustrating the robust ROS generation, which is further supported by the confocal laser scanning microscopy (CLSM) imaging (Fig. 4L). Furthermore, the Russell mechanism–mediated $^1O_2$ generation was supported by CLSM imaging. An evident green fluorescence manifests the $^1O_2$ existence, indicating the GSH consumption during the redox reaction with CPMNSs, resulting in effective ROS production for further LPO (Fig. 4M).

In vitro LPO evaluation

Encouraged by the above-proved ROS generation, GSH depletion, and GPX4 deactivation, LPO performance was further evaluated in vitro. In general, a typical LPO process involves three steps: First, emerging ROS attacks unsaturated lipid to form lipid radical at the initiation stage; then, lipid peroxyradical is produced in the presence of oxygen at the propagation period. Last, the LOOH breaks down into smaller molecular by-products containing malondialdehyde (MDA) at the termination process (Fig. 5A) (*13*, *40*). As a LPO inhibitor (*41*), Lip-1 can diminish the cellular damage caused by oxidative stress upon the treatment with CPMNSs (Fig. 5B). In addition, vitamin E (VE) is able to mitigate the CPMNS-caused cell injury on account of the effective LPO inhibition by eliminating the lipid peroxyradical (Fig. 5C) (*42*). The LOOH can be easily cleaved into small organic pieces, in which MDA fragment is regarded as one of the primary LPO end-products of unsaturated lipid. As depicted in Fig. 5 (D and E), the MDA amounts in the CPMNS-treated group increase notably with the increases of CPMNS concentrations and incubation durations, and that of CPMNSs (150 μg ml^{-1}) become 3.4 times as large as that in the control group, illustrating the build-up of LPO for activating ferroptosis.

C11-BODIPY$^{581/591}$, an oxidation-sensitive and LPO-specific fluorescent probe, is capable of accumulating at the cell membrane. Upon C11-BODIPY$^{581/591}$ oxidizing, the maximum emission peak will shift from 590 nm (red) to 510 nm (green) and maintain the intrinsic lipophilicity, facilitating the membrane LPO detection (*43*). CLSM images in Fig. 5 (F and G) reveal the red fluorescence decay and green fluorescence intensification at the increased therapeutic CPMNS dosage and time duration in the CPMNS-treated groups, demonstrating the desired CPMNS-stimulated LPO.

Ferroptosis assay in mice model

Inspired by the desired in vitro ferroptosis therapeutic effect, the in vivo ferroptosis assay in the mice model was conducted. The hemocompatibility and histocompatibility of CPMNSs were initially evaluated. The serum biochemistry and routine blood indexes exhibit negligible inflammation both in the control and CPMNS-treated groups in 28 days (fig. S13). The histological observations of major organs (heart, liver, spleen, lung, and kidney) display negligible acute pathological toxicities and adverse effects during the treatment duration for the control or treated groups (fig. S14). These results exhibit that CPMNSs are of high biocompatibility for further safe in vivo tumor nanomedicine. Furthermore, the time-dependent Co biodistributions of CPMNSs at tumor and major organs were measured, and an effective accumulation of CPMNSs was observed at the tumor site, in addition to those in reticuloendothelial systems including liver, lung, and kidney, ensuring the following ferroptosis tumor therapy (fig. S15).

The in vivo ferroptosis-augmented antitumor efficacy of CPMNSs has been demonstrated on 4T1 xenograft tumor–bearing mice. As depicted in Fig. 6A of the treatment protocol, mice models were under intravenous and intratumoral administration of CPMNSs (10 mg kg^{-1}) on 0 and 7 days. When the tumor sizes reached about 100 mm^3, these tumor-bearing mice were randomly divided into four groups, followed by treatments with the following: (i) untreated (control), (ii) CPMNSs with intravenous administration (CPMNSs i.v.), (iii) CPMNSs with intratumoral administration (CPMNSs i.t.), and (iv) CPMNSs with intratumoral administration + DFOM (CPMNSs i.t. + DFOM). To validate the ferroptosis, iron chelating agent of DFOM was additionally intraperitoneally administrated every 4 days for ferroptosis inhibition following the intratumoral administration of CPMNSs. During the therapeutic period, all the mice feature negligible weight changes, confirming the negligible negative impacts of these treatments on the health of mice (fig. S16). During the 16 days of observation, a fast increase of tumor size in untreated group was visualized, while the tumor growths in CPMNSs i.v. and CPMNSs i.t. + DFOM groups were only slightly inhibited (Fig. 6B). It is noted that the tumor growth was notably suppressed in the CPMNSs i.t. group, in which the antineoplastic effect (growth inhibition rate) is 1.9 times that of the CPMNSs i.t. + DFOM group (Fig. 6B). The individual tumor growth behaviors of mice in each group feature similar but notably distinguishable tendencies, demonstrating the effective ferroptosis efficacy by CPMNSs (Fig. 6G). Tumor tissues were harvested from the mice and stained for hematoxylin and eosin (H&E) evaluation, which validates the tumor tissue injury to varying degrees by CPMNS treatments (Fig. 6F). Simultaneously, more terminal deoxynucleotidyl transferase–mediated deoxyuridine triphosphate nick end labeling (TUNEL)–defined apoptosis cells can be found as well after CPMNS treatment because ferroptosis is usually closely connected with apoptosis (*44*). Consistently, as a result of tumor tissue damage, the therapeutic groups show much reduced proliferation capacity as can be found in Ki-67 slices, indicating the effective tumor therapeutic effect of CPMNSs.

The ROS proliferation and GPX4 deactivation performances of CPMNS-stimulated ferroptosis were further evaluated. The ROS presents green fluorescence in both CPMNSs i.v. and CPMNSs i.t. groups by DCFH-DA staining, which is notably distinguishable from the control group (Fig. 6C), evidencing ROS production in the tumor microenvironment by CPMNS treatment. Furthermore, the GPX4 activity is also affected by CPMNS treatment, as indicated by the immunohistochemical expression decrease to a certain extent (Fig. 6D). On the basis of the favorable ROS generation and GPX4 deactivation performances, the supposed LPO was further checked. As expected, the C11-BODIPY$^{581/591}$ dye–marked and green-stained oxidation fluorescence show notably enhanced intensity in CPMNSs i.v. and CPMNSs i.t. groups in comparison to that of the control, further illustrating the effectiveness of CPMNSs in cancer cell ferroptosis (Fig. 6C). Moreover, all untreated tumor-bearing mice of the control group died in 16 days (Fig. 6E); in contrast, all the mice in the CPMNSs i.t. group were kept alive in 21 days.

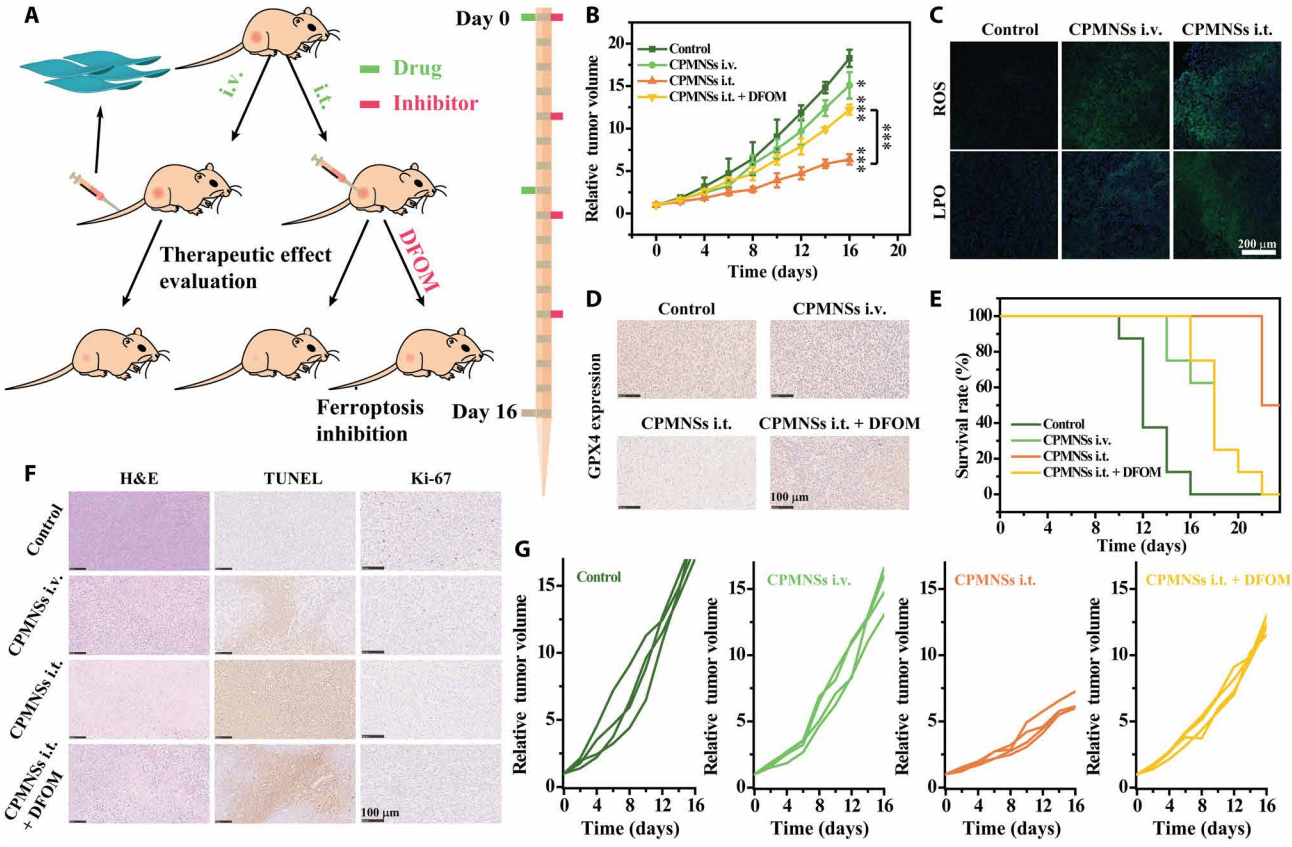

Fig. 6. In vivo ferroptosis assay. (**A**) Schematics of CPMNS-induced ferroptosis evaluation. (**B**) Tumor growth curves of tumor-bearing mice subject to diverse treatments. (**C**) Tumor tissue slices costained with DCFH-DA and 4′,6-diamidino-2-phenylindole (DAPI; top) and C11-BODIPY$^{581/591}$ and DAPI (bottom). (**D**) GPX4 immunohistochemical analysis of tumor tissues after different treatments as noted. (**E**) Survival rate of experimental mice receiving different treatments. (**F**) H&E, TUNEL, and Ki-67 slices for the ferroptosis analysis of tumor tissues after different treatments. (**G**) Growth curve recorded from each mouse in all groups as noted. *$P < 0.05$ and ***$P < 0.001$ compared with control group. ***$P < 0.001$ compared with CPMNSs i.t. and CPMNSs i.t. + DFOM.

DISCUSSION

In summary, a synergetic tumor ferroptosis–like strategy by using a nonferrous agent has been developed on the basis of the GSH consumption–promoted ROS production and GPX4 deactivation. The redox reaction between as-established CPMNS nanoplatform and the overexpressed GSH within tumors results in the concurrent GSH depletion, Mo^{6+} reduction to Mo^{5+} of CPMNSs, and the Co^{2+} release from the structure-collapsed CPMNSs. Respectively, the GSH consumption favors the GPX4 deactivation; Mo^{6+} reduction to Mo^{5+} triggers the $^1O_2$ formation by reacting with H_2O_2 via a Russell mechanism, and the released Co^{2+} catalyzes the Fenton-like reaction with endogenous H_2O_2 for producing ·OH radicals under the assistance of physiological HCO_3^-. As a result, the LPO is intensified by both ROS production and GSH/GPX4 depletion/deactivation, leading to notable ferroptosis of cancer cells and marked suppression of tumor growth. Such a paradigm not only presents an effective ferroptosis strategy but also provides a useful antioxidant-regulation way to intensify the oxidative damages of tumors by ROS.

MATERIALS AND METHODS

Materials

Cobalt acetate [$Co(Ac)_2$], ammonium phosphomolybdate hydrate (PMA), oleylamine (OA), ethanolamine (EA), DMPO, TEMP, DPBF, GSH, DTNB, NAC, and EDTA were purchased from Adamas-beta Inc. (Shanghai, China). Acetone and H_2O_2 were obtained from Sinopharm Chemical Reagent Co. Ltd. (Shanghai, China). Necrostatin-1, rhodamine B, 3-methyladenine (3-MA), Z-VAD-FMK, MB, polyethylene-polypropylene glycol (Pluronic F127; Mn ~ 13,000), VE, Lip-1, and DFOM were obtained from Shanghai Macklin Biochemical Co. Ltd. (Shanghai, China). SOSG assay kit was purchased from BestBio Co. Ltd. (Shanghai, China). C11-BODIPY$^{581/591}$ was purchased from Thermo Fisher Scientific Inc. (Waltham, USA). Reactive Oxygen Species Assay Kit, Glutathione Peroxidase Assay Kit, Cell Counting Kit-8 (CCK-8), BCA Protein Assay Kit, Lipid Peroxidation MDA Assay Kit, DAPI (4′,6-diamidino-2-phenylindole), and GSH and GSSG Assay Kit were purchased from Beyotime Institute of Biotechnology (Jiangsu, China). Anti-Glutathione Peroxidase 4 antibody (EPNCIR144; ab125066) was obtained from Abcam Inc. (Shanghai, China).

Synthesis and characterization of CPMNSs

CPMNSs were synthesized referring to the reported method (*31*). Briefly, 0.03 g of PMA and 0.12 g of $Co(Ac)_2$ were dissolved in a mixture of 3 ml each of acetone, OA, and EA, further stirring for 10 min. The mixture reacted at 180°C for 6 hours in a Teflon-lined stainless steel autoclave. The final product was washed by ethanol and cyclohexane.

For modification, 10 ml of chloroform solution containing 100 mg of Pluronic F127 and 10 mg of CPMNSs sonicated for 30 min, and the chloroform was evaporated through a rotary evaporator at 45°C for 2 hours under vacuum. The residual solid was washed by PBS (pH 7.4).

The morphology of CPMNSs was observed by field-emission transmission electron microscopy (TEM; JEM-2100F) and field-emission scanning electron microscope (SEM; Zeiss Gemini 450), where CPMNSs dispersed in ethanol/cyclohexane (volume ratio of 1/1) solution were dropped on TEM grid and silicon plate for TEM and SEM morphology observation, respectively. The thickness of CPMNSs was determined by atomic force microscopy (Multimode 8) where the ethanol/cyclohexane solution containing CPMNSs was placed on silicon plate for sample preparation. The chemical composition was evaluated by XPS (AXIS Supra) and XRD (Ultima IV). The surface modification of CPMNSs was confirmed by FTIR spectrum (NEXUS670). The optical absorption assay was evaluated by ultraviolet–visible–near-infrared spectrophotometers (UV-3600 Plus). The hydrated diameter of CPMNSs was detected by Malvern Nano ZS90.

Fenton-like–mediated ·OH production of CPMNSs

After immersing in PBS buffer (pH 6.5, with 5% CO_2) for about 3 hours in CPMNSs, MB (10 μg ml^{-1}), $NaHCO_3$ (25 mM), H_2O_2 (10 mM), and CPMNSs (100 μg ml^{-1}) were mixed and reacted for 10 min. The MB degradation was detected by the characteristic absorption change at 665 nm. Moreover, the ·OH generation was further monitored by electron paramagnetic resonance (ESR) spectrum (EMXplus) using DMPO-trapping agent where the immerse time of CPMNSs was prolonged to 24 hours with 10 mM $NaHCO_3$ and 4 mM H_2O_2.

GSH depletion capacity of CPMNSs

The GSH amount was detected by DTNB at the absorption of 412 nm. Briefly, GSH (1 mM) and CPMNSs (50 μg ml^{-1}) mixture reacted for 3 hours; then, DTNB (0.5 mM) was added to detect the residual GSH, and H_2O_2 (1 mM) as a GSH depletion inducer was also evaluated. Moreover, the time (10 min and 3 hours)– and CPMNS concentration (12.5, 25, 50, and 100 μg ml^{-1})–dependent GSH depletion was also determined.

·OH generation capacity with GSH addition

GSH (0.5, 1, and 2 mM) was first interacted with CPMNSs (100 μg ml^{-1}) in PBS (pH 6.5, with 5% CO_2) buffer for 30 min and then added with MB (10 μg ml^{-1}), H_2O_2 (10 mM), and $NaHCO_3$ (25 mM) reacting for 10 min. The MB degradation was detected at the absorbance of 665 nm.

GSH reduction–mediated $^1O_2$ generation of CPMNSs

The mixture of GSH (10 mM) and CPMNSs (100 μg ml^{-1}) reacted overnight. SOSG (10 μl; from SOSG assay kit), 200 μl of H_2O_2 (10 mM), and 400 μl of mixture were added with 1.4 ml of PBS buffer. The change of SOSG fluorescence intensity was monitored by the fluorescence spectrometer (FLS980) with excitation (Ex)/emission (Em) of 488/525 nm. Besides, DPBF (20 μg/ml) was further used to monitor the $^1O_2$ generation at the declined absorption of 419 nm. For ESR assay, 100 μl of H_2O_2 (10 mM), 600 μl of mixture, and 300 μl of PBS were added with TEMP-trapping agent for 10 min reaction.

Co ion release

CPMNSs (3 mg) were fastened by dialysis bag and put into a centrifuge tube with 15 ml of solution, which were divided into three groups of (i) PBS (pH 7.4), (II) PBS (pH 6.5), and (III) PBS + GSH (pH 6.5, 10 mM GSH). The reaction solution (1 ml) was taken out at the predetermined time (10 min; 30 min; and 1, 2, 4, 6, 12, 24, and 36 hours) for Co^{2+} detection. The Co amount was determined by the inductively coupled plasma optical emission spectroscopy (5100 ICP-OES). In 10 min of reaction, the solution drops of group II and group III were immediately added onto TEM grids for morphology observation.

Reversible redox property of CPMNSs analysis

For electrochemical analysis, 5 mg of CPMNSs, 1 ml of H_2O, and 1 ml of ethanol were mixed and sonicated for 30 min; then, 50 μl of Nafion was added and sequentially sonicated for 10 min. The mixture (5 μl) was drooped onto glass carbon electrode. Ag/AgCl was selected as reference electrode, and carbon rod was selected as counter electrode. For cobalt analysis, PBS (pH 6.5) and $NaHCO_3/CO_2$ were set as electrolyte solution. For molybdenum analysis, 0.1 M H_2SO_4 was selected as electrolyte solution.

For the detection of valence states of Mo element, CPMNSs (100 μg ml^{-1}) were sequentially added with GSH (20 mM), GSH (20 mM) + H_2O_2 (40 mM), and GSH (20 mM) + H_2O_2 (40 mM) + GSH (40 mM), respectively. Then, the Mo valence state change was detected by XPS analysis.

Cellular culture

Mammary carcinoma cell (4T1) was purchased from Biochemistry and Cell Biology Institute from Shanghai, Chinese Academy of Sciences. The cells were incubated with RPMI 1640 medium with streptomycin (100 μg ml^{-1}), penicillin (100 U/ml), and 10% FBS and surrounded with 5% CO_2 at 37°C.

Cellular uptake assay

The CLSM dish–adhered 4T1 cells were incubated with rhodamine B–labeled CPMNSs. In different time intervals (1, 2, and 4 hours) of coincubation, the cell nucleus was stained by DAPI, and the progress of cell uptake was observed by CLSM (FV1000 from Olympus Company, Japan).

Cellular ferroptosis inhibition assay

The cell killing capacity of CPMNSs was first evaluated where the well-cultured adherent 4T1 cells were incubated with CPMNSs (25, 50, 100, 125, 150, 175, 200, and 250 μg/ml) for 24 hours, and then, the cell viability was evaluated by CCK-8.

For ferroptosis assay, 4T1 cells were preincubated in 96-well plate for 24 hours and then coincubated with CPMNSs (150 μg ml^{-1}) and numerous types of ferroptosis inhibitors including DFOM (300, 400, and 800 μM), GSH (0.625, 1.25, and 2.5 mM), NAC (3, 4, and 5 mM), Lip-1 (2, 4, and 8 μM), VE (12.5, 25, and 50 μM), and EDTA (200, 400, and 600 μM). After being cultured for another 24 hours, the cell viability was determined by CCK-8.

Cellular necroptosis, apoptosis, and autophagy inhibition assays

The adherent 4T1 cells were coincubated with CPMNSs (150 μg ml^{-1}) and varied cell death pathway inhibitors for 24 hours, including 3-MA (125, 250, and 500 μM), necrostatin-1 (125, 250, and 500 μM),

and Z-VAD-FMK (125, 250 and 500 μM). The cell viabilities of 4T1 cells were detected by CCK-8.

Intracellular GSH, GPX4, and MDA assay

Six-well plate–adhered 4T1 cells were incubated with various concentrations of CPMNSs (50, 100, and 150 μg ml^{-1}) for 12 hours or different times (3, 6, and 9 hours) with the same concentration (150 μg ml^{-1}). The GSH amount was evaluated using GSH assay kit; the GPX4 activity was measured using GSH peroxidase assay kit, and MDA amount was monitored using LPO MDA assay kit. In addition, the protein concentration of cellular samples was assayed using BCA protein assay kit.

CLSM of intracellular ROS and LPO assay

4T1 cells were seeded into confocal-specific dishes for 24 hours; after that, they were incubated with various concentrations of CPMNSs (50, 100, and 150 μg ml^{-1}) for 12 hours or different times (3, 6, and 9 hours) with the same concentration (150 μg ml^{-1}). For ROS evaluation, at the predetermined time, the culture medium was replaced by fresh DCFH-DA–containing medium (10 μM) for 30 min. The ROS fluorescence was observed by CLSM with Ex/Em of 488/525 nm, and the ROS generation was further evaluated by flow cytometry (BD LSRFortessa). For $^1O_2$ assay, the culture medium was replaced by SOSG probe and incubated for 2 hours; then, the fluorescence was detected with Ex/Em of 488/525 nm. For LPO assay, cells were incubated with C11-$BODIPY^{581/591}$ fluorescent probe (10 μM) for 30 min.

Animal treatment

Female Kunming (KM) mice and BALB/c nude mice were obtained from Shanghai SLAC Laboratory Animal Center. All animal studies conformed to the guidelines of the Animal Care Ethics Commission of Shanghai Tenth People's Hospital, Tongji University School of Medicine.

In vivo biocompatible assay

KM mice were randomly divided into six groups (n = 4), where groups I to III were intravenously injected with CPMNSs (15 mg kg^{-1}) keeping feed for 1, 14, and 28 days, and groups IV to VI were intravenously injected with PBS keeping feed for 1, 14, and 28 days. At the scheduled time, the corresponding blood was obtained for blood routine and blood biochemistry evaluation. The major organs of heart, liver, spleen, lung, and kidney were harvested for H&E slices.

In vivo biodistribution assay

4T1 tumor–bearing mice were intravenously injected with CPMNSs (10 mg kg^{-1}). At the planned time points (6 and 12 hours), the major tissues and tumor were obtained and digested with aqua regia. The Co amount was detected by ICP-OES analysis. The biodistribution amount of CPMNSs (injected dose per gram) was calculated as (the Co amount of tissue)/(the Co amount of injection dose)/(tissue mass).

In vivo ferroptosis therapeutic effect assay

4T1 cells were subcutaneously administrated into BALB/c mice for tumor mode. After reaching about 100 mm^3 of tumor volume, the bearing BALB/c mice were randomly divided into four groups. Group I underwent nontreatment (control). Group II was intravenously injected with CPMNSs (10 mg kg^{-1}) at day 0 and day 7 (CPMNSs i.v.). Group III was intratumorally administrated with CPMNSs (10 mg kg^{-1}) at day 0 and day 7 (CPMNSs i.t.). In addition to the same treatment as group III, group IV also intraperitoneally received DFOM (20 mg kg^{-1}) at days 0, 4, 8, and 12 (CPMNSs i.v. + DFOM). The tumor volume and body weight were recorded every 2 days for 16 days. After ending the treatment, the tumors were captured for H&E slice, GPX4, antigen Ki-67, and TUNEL immunohistochemistry analyses. For survival rate assay, the mice were considered dead when tumor volume arrived at 1500 mm^3.

In vivo ROS and LPO assay

The tumor-bearing BALB/c mice were divided into three groups at random: group I without any treatment (control) and group II (CPMNSs i.v.) and group III (CPMNSs i.t.) were intravenously and intratumorally injected with CPMNSs (10 mg kg^{-1}), respectively. After being administrated for 24 hours, the tumor site was in situ injected with 100 μl of DCFH-DA probe (10 μM) or 100 μl of C11-$BODIPY^{581/591}$ dye (10 μM) for another 30 min. Then, the tumor was sliced for CLSM imaging.

Statistical analysis

The significant difference of the experimental data was evaluated through one-way analysis of variance (ANOVA) (using OriginPro 8.5 software). The calculated probability (P) was distinguished between $^*P < 0.05$, $^{**}0.001 < P < 0.01$, and $^{***}P < 0.001$.

SUPPLEMENTARY MATERIALS

Supplementary material for this article is available at https://science.org/doi/10.1126/sciadv.abj8833

REFERENCES AND NOTES

1. S. J. Dixon, K. M. Lemberg, M. R. Lamprecht, R. Skouta, E. M. Zaitsev, C. E. Gleason, D. N. Patel, A. J. Bauer, A. M. Cantley, W. S. Yang, B. Morrison, B. R. Stockwell, Ferroptosis: An iron-dependent form of nonapoptotic cell death. *Cell* **149**, 1060–1072 (2012).
2. D. Tang, X. Chen, R. Kang, G. Kroemer, Ferroptosis: Molecular mechanisms and health implications. *Cell Res.* **31**, 107–125 (2020).
3. X. Chen, R. Kang, G. Kroemer, D. Tang, Broadening horizons: The role of ferroptosis in cancer. *Nat. Rev. Clin. Oncol.* **18**, 280–296 (2021).
4. L. Nathell, A. Gohlke, S. Wohlfeil, Reported severe hypersensitivity reactions after intravenous iron administration in the European Economic Area (EEA) before and after implementation of risk minimization measures. *Drug Saf.* **43**, 35–43 (2020).
5. M. Auerbach, I. Macdougall, The available intravenous iron formulations: History, efficacy, and toxicology. *Hemodial. Int.* **21**, S83–S92 (2017).
6. L. McCulley, K. Gelperin, S. Bird, S. Harris, C. Wang, P. Waldron, Reports to FDA of fatal anaphylaxis associated with intravenous iron products. *Am. J. Hematol.* **91**, E496–E497 (2016).
7. M. Lu, M. H. Cohen, D. Rieves, R. Pazdur, FDA report: Ferumoxytol for intravenous iron therapy in adult patients with chronic kidney disease. *Am. J. Hematol.* **85**, 315–319 (2010).
8. M. A. Badgley, D. M. Kremer, H. C. Maurer, K. E. DelGiorno, H.-J. Lee, V. Purohit, I. R. Sagalovskiy, A. Ma, J. Kapilian, C. E. M. Firl, A. R. Decker, S. A. Sastra, C. F. Palermo, L. R. Andrade, P. Sajjakulnukit, L. Zhang, Z. P. Tolstyka, T. Hirschhorn, C. Lamb, T. Liu, W. Gu, E. S. Seeley, E. Stone, G. Georgiou, U. Manor, A. Iuga, G. M. Wahl, B. R. Stockwell, C. A. Lyssiotis, K. P. Olive, Cysteine depletion induces pancreatic tumor ferroptosis in mice. *Science* **368**, 85–89 (2020).
9. D. Anastasiou, G. Poulogiannis, J. M. Asara, M. B. Boxer, J.-k. Jiang, M. Shen, G. Bellinger, A. T. Sasaki, J. W. Locasale, D. S. Auld, C. J. Thomas, M. G. Vander Heiden, L. C. Cantley, Inhibition of pyruvate kinase M2 by reactive oxygen species contributes to cellular antioxidant responses. *Science* **334**, 1278–1283 (2011).
10. C. Zhang, W. Bu, D. Ni, S. Zhang, Q. Li, Z. Yao, J. Zhang, H. Yao, Z. Wang, J. Shi, Synthesis of iron nanometallic glasses and their application in cancer therapy by a localized Fenton reaction. *Angew. Chem. Int. Ed.* **55**, 2101–2106 (2016).
11. H. Lin, Y. Chen, J. Shi, Nanoparticle-triggered in situ catalytic chemical reactions for tumour-specific therapy. *Chem. Soc. Rev.* **47**, 1938–1958 (2018).
12. B. Yang, Y. Chen, J. Shi, Nanocatalytic medicine. *Adv. Mater.* **31**, 1901778 (2019).
13. B. Hassannia, P. Vandenabeele, T. Vanden Berghe, Targeting ferroptosis to iron out cancer. *Cancer Cell* **35**, 830–849 (2019).

14. X. Jiang, B. R. Stockwell, M. Conrad, Ferroptosis: Mechanisms, biology and role in disease. *Nat. Rev. Mol. Cell Biol.* **22**, 266–282 (2021).
15. L. Gao, Y. Zhang, L. Zhao, W. Niu, Y. Tang, F. Gao, P. Cai, Q. Yuan, X. Wang, H. Jiang, X. Gao, An artificial metalloenzyme for catalytic cancer-specific DNA cleavage and operando imaging. *Sci. Adv.* **6**, eabb1421 (2020).
16. L.-S. Lin, J. Song, L. Song, K. Ke, Y. Liu, Z. Zhou, Z. Shen, J. Li, Z. Yang, W. Tang, G. Niu, H.-H. Yang, X. Chen, Simultaneous Fenton-like ion delivery and glutathione depletion by MnO_2-based nanoagent to enhance chemodynamic therapy. *Angew. Chem. Int. Ed.* **57**, 4902–4906 (2018).
17. X. Lu, S. Gao, H. Lin, L. Yu, Y. Han, P. Zhu, W. Bao, H. Yao, Y. Chen, J. Shi, Bioinspired copper single-atom catalysts for tumor parallel catalytic therapy. *Adv. Mater.* **32**, 2002246 (2020).
18. S. Dong, Y. Dong, T. Jia, S. Liu, J. Liu, D. Yang, F. He, S. Gai, P. Yang, J. Lin, GSH-depleted nanozymes with hyperthermia-enhanced dual enzyme-mimic activities for tumor nanocatalytic therapy. *Adv. Mater.* **32**, 2002439 (2020).
19. B. Ma, S. Wang, F. Liu, S. Zhang, J. Duan, Z. Li, Y. Kong, Y. Sang, H. Liu, W. Bu, L. Li, Self-assembled copper–amino acid nanoparticles for in situ glutathione "AND" H_2O_2 sequentially triggered chemodynamic therapy. *J. Am. Chem. Soc.* **141**, 849–857 (2019).
20. L. He, G. Huang, H. Liu, C. Sang, X. Liu, T. Chen, Highly bioactive zeolitic imidazolate framework-8–capped nanotherapeutics for efficient reversal of reperfusion-induced injury in ischemic stroke. *Sci. Adv.* **6**, eaay9751 (2020).
21. X. Zhong, X. Wang, L. Cheng, Y. A. Tang, G. Zhan, F. Gong, R. Zhang, J. Hu, Z. Liu, X. Yang, GSH-depleted $PtCu_3$ nanocages for chemodynamic- enhanced sonodynamic cancer therapy. *Adv. Funct. Mater.* **30**, 1907954 (2020).
22. J.-S. Lan, L. Liu, R.-F. Zeng, Y.-H. Qin, J.-W. Hou, S.-S. Xie, S. Yue, J. Yang, R. J. Y. Ho, Y. Ding, T. Zhang, Tumor-specific carrier-free nanodrugs with GSH depletion and enhanced ROS generation for endogenous synergistic anti-tumor by a chemotherapy-photodynamic therapy. *Chem. Eng. J.* **407**, 127212 (2021).
23. W. S. Yang, R. SriRamaratnam, M. E. Welsch, K. Shimada, R. Skouta, V. S. Viswanathan, J. H. Cheah, P. A. Clemons, A. F. Shamji, C. B. Clish, L. M. Brown, A. W. Girotti, V. W. Cornish, S. L. Schreiber, B. R. Stockwell, Regulation of ferroptotic cancer cell death by GPX4. *Cell* **156**, 317–331 (2014).
24. J. K. Eaton, L. Furst, R. A. Ruberto, D. Moosmayer, A. Hilpmann, M. J. Ryan, K. Zimmermann, L. L. Cai, M. Niehues, V. Badock, A. Kramm, S. Chen, R. C. Hillig, P. A. Clemons, S. Gradl, C. Montagnon, K. E. Lazarski, S. Christian, B. Bajrami, R. Neuhaus, A. L. Eheim, V. S. Viswanathan, S. L. Schreiber, Selective covalent targeting of GPX4 using masked nitrile-oxide electrophiles. *Nat. Chem. Biol.* **16**, 497–506 (2020).
25. J. Li, F. Cao, H.-l. Yin, Z.-j. Huang, Z.-t. Lin, N. Mao, B. Sun, G. Wang, Ferroptosis: Past, present and future. *Cell Death Dis.* **11**, 88 (2020).
26. B. R. Stockwell, J. P. Friedmann Angeli, H. Bayir, A. I. Bush, M. Conrad, S. J. Dixon, S. Fulda, S. Gascón, S. K. Hatzios, V. E. Kagan, K. Noel, X. Jiang, A. Linkermann, M. E. Murphy, M. Overholtzer, A. Oyagi, G. C. Pagnussat, J. Park, Q. Ran, C. S. Rosenfeld, K. Salnikow, D. Tang, F. M. Torti, S. V. Torti, S. Toyokuni, K. A. Woerpel, D. D. Zhang, Ferroptosis: A regulated cell death nexus linking metabolism, redox biology, and disease. *Cell* **171**, 273–285 (2017).
27. C.-C. Xue, M.-H. Li, Y. Zhao, J. Zhou, Y. Hu, K.-Y. Cai, Y. Zhao, S.-H. Yu, Z. Luo, Tumor microenvironment-activatable Fe-doxorubicin preloaded amorphous $CaCO_3$ nanoformulation triggers ferroptosis in target tumor cells. *Sci. Adv.* **6**, eaax1346 (2020).
28. Y. Jiang, X. Zhao, J. Huang, J. Li, P. K. Upputuri, H. Sun, X. Han, M. Pramanik, Y. Miao, H. Duan, K. Pu, R. Zhang, Transformable hybrid semiconducting polymer nanozyme for second near-infrared photothermal ferrotherapy. *Nat. Commun.* **11**, 1857 (2020).
29. C. Zhang, Z. Liu, Y. Zhang, L. Ma, E. Song, Y. Song, "Iron free" zinc oxide nanoparticles with ion-leaking properties disrupt intracellular ROS and iron homeostasis to induce ferroptosis. *Cell Death Dis.* **11**, 183 (2020).
30. S. Wang, H. Liao, F. Li, D. Ling, A mini-review and perspective on ferroptosis-inducing strategies in cancer therapy. *Chin. Chem. Lett.* **30**, 847–852 (2019).
31. B. Akram, W. Shi, H. Zhang, S. Ullah, M. Khurram, X. Wang, Free-standing CoO-POM Janus-like ultrathin nanosheets. *Angew. Chem. Int. Ed.* **59**, 8497–8501 (2020).
32. A. Y. Satoh, J. E. Trosko, S. J. Masten, Methylene blue dye test for rapid qualitative detection of hydroxyl radicals formed in a Fenton's reaction aqueous solution. *Environ. Sci. Technol.* **41**, 2881–2887 (2007).
33. A. Xu, X. Li, S. Ye, G. Yin, Q. Zeng, Catalyzed oxidative degradation of methylene blue by in situ generated cobalt (II)-bicarbonate complexes with hydrogen peroxide. *Appl. Catal. Environ.* **102**, 37–43 (2011).
34. C. Zhang, W. Bu, D. Ni, C. Zuo, C. Cheng, Q. Li, L. Zhang, Z. Wang, J. Shi, A polyoxometalate cluster paradigm with self-adaptive electronic structure for acidity/reducibility-specific photothermal conversion. *J. Am. Chem. Soc.* **138**, 8156–8164 (2016).
35. Y. Yang, Y. Lu, P. L. Abbaraju, I. Azimi, C. Lei, J. Tang, M. Jambhrunkar, J. Fu, M. Zhang, Y. Liu, C. Liu, C. Yu, Stepwise degradable nanocarriers enabled cascade delivery for synergistic cancer therapy. *Adv. Funct. Mater.* **28**, 1800706 (2018).
36. C. Wang, F. Cao, Y. Ruan, X. Jia, W. Zhen, X. Jiang, Specific generation of singlet oxygen through the Russell mechanism in hypoxic tumors and GSH depletion by Cu-TCPP nanosheets for cancer therapy. *Angew. Chem. Int. Ed.* **58**, 9846–9850 (2019).
37. G. Liu, J. Zhu, H. Guo, A. Sun, P. Chen, L. Xi, W. Huang, X. Song, X. Dong, Mo_2C-derived polyoxometalate for NIR-II photoacoustic imaging-guided chemodynamic/photothermal synergistic therapy. *Angew. Chem. Int. Ed.* **58**, 18641–18646 (2019).
38. H. U. Simon, A. Haj-Yehia, F. Levi-Schaffer, Role of reactive oxygen species (ROS) in apoptosis induction. *Apoptosis* **5**, 415–418 (2000).
39. D. Ezeriņa, Y. Takano, K. Hanaoka, Y. Urano, T. P. Dick, *N*-acetyl cysteine functions as a fast-acting antioxidant by triggering intracellular H_2S and sulfane sulfur production. *Cell Chem. Biol.* **25**, 447–459.e4 (2018).
40. V. B. O'Donnell, M. Aldrovandi, R. C. Murphy, G. Krönke, Enzymatically oxidized phospholipids assume center stage as essential regulators of innate immunity and cell death. *Sci. Signal.* **12**, eaau2293 (2019).
41. O. Zilka, R. Shah, B. Li, J. P. Friedmann Angeli, M. Griesser, M. Conrad, D. A. Pratt, On the mechanism of cytoprotection by ferrostatin-1 and liproxstatin-1 and the role of lipid peroxidation in ferroptotic cell death. *ACS Cent. Sci.* **3**, 232–243 (2017).
42. A. D. Allu, B. Simancas, S. Balazadeh, S. Munné-Bosch, Defense-related transcriptional reprogramming in vitamin E-deficient arabidopsis mutants exposed to contrasting phosphate availability. *Front. Plant Sci.* **8**, 1396 (2017).
43. L.-S. Lin, T. Huang, J. Song, X.-Y. Ou, Z. Wang, H. Deng, R. Tian, Y. Liu, J.-F. Wang, Y. Liu, G. Yu, Z. Zhou, S. Wang, G. Niu, H.-H. Yang, X. Chen, Synthesis of copper peroxide nanodots for H_2O_2 self-supplying chemodynamic therapy. *J. Am. Chem. Soc.* **141**, 9937–9945 (2019).
44. X. Meng, J. Deng, F. Liu, T. Guo, M. Liu, P. Dai, A. Fan, Z. Wang, Y. Zhao, Triggered all-active metal organic framework: Ferroptosis machinery contributes to the apoptotic photodynamic antitumor therapy. *Nano Lett.* **19**, 7866–7876 (2019).

Acknowledgments

Funding: This work was supported by the National Natural Science Foundation of China (grant nos. 52002391 and 21835007), Key Research Program of Frontier Sciences, Chinese Academy of Sciences (grant no. ZDBS-LY-SLH029), China Postdoctoral Science Foundation (grant no. 2019M660098), and Science Foundation for Youth Scholar of State Key Laboratory of High Performance Ceramics and Superfine Microstructures (grant no. SKL201906). **Author contributions:** C.W., H.L., and J.S. co-designed the experiment. C.W., Z.C., L.C., and D.X. were responsible for the preparation and characterization of CPMNSs. Z.L and H.L. participated in cell and animal experiments. C.W., H.L., and J.S. wrote the manuscript. **Competing interests:** The authors declare that they have no competing interests. **Data and materials availability:** All data needed to evaluate the conclusions in the paper are present in the paper and/or the Supplementary Materials.

Submitted 9 June 2021
Accepted 29 July 2021
Published 22 September 2021
10.1126/sciadv.abj8833

Citation: C. Wu, Z. Liu, Z. Chen, D. Xu, L. Chen, H. Lin, J. Shi, A nonferrous ferroptosis-like strategy for antioxidant inhibition–synergized nanocatalytic tumor therapeutics. *Sci. Adv.* **7**, eabj8833 (2021).